3D printed Helmholtz microstreaming structures: analysis of bubble dynamics, bulk fluid disturbance, and resiliency in non-quiescent conditions

Kieran Fung^a, Shouhong Fan^a, Thomas J. Kolibaba^c, Benjamin W. Caplins^c, Jason P. Killgore^c, Xiaoyun Ding^{a,b*}, Yifu Ding^{a*}

^a Membrane Science, Engineering and Technology Center

Paul M. Rady Department of Mechanical Engineering University of Colorado, Boulder, CO, 80309

^b Biomedical Engineering Program, University of Colorado Boulder, Boulder, CO, 80309 ^c Applied Chemicals and Materials Division, National Institute of Standards and Technology, Boulder, CO, 80305

Abstract

Microstreaming of acoustically excited bubbles presents great potential to mitigate fouling for membrane technologies. However, the acoustic streaming in bulk fluids under membrane separation conditions is not well explored. In this work, we investigate the microstreaming of 3D printed Helmholtz-like bubble-trapping-structures (BTSs) under no flow, pressurized, and crossflow conditions that are relevant to membrane applications. Trapped bubbles are shown to generate formidable microstreaming that spans millimeter distances with velocity as high as 125 mm/s in bulk aqueous medium. However, complex mode shapes of the bubble oscillation and bubble growth were observed during frequency sweep. As a result, the streaming velocity decreases by 76 % over 30 minutes, under single frequency excitation. The BTS displayed effective microstreaming under hydrostatic pressure up to 9.0 kPa, and under crossflow velocity up to 0.2 mm/s, where the microstreaming zone reduced to < 1 mm. The results provide the operation window, as well as challenges, for future integration of the BTS into bulk membrane separation processes.

Keywords: 3D Printing, Microstreaming, Bubble Oscillations, Particle Manipulation, Membrane Cleaning

*Corresponding Author. Paul M. Rady Department of Mechanical Engineering University of Colorado, Boulder, CO 80309-0427, USA.

1. Introduction

Fouling is an inherent consequence of separating mixture constituents with a size selective membrane [1], and remains one of the biggest obstacles faced in the field of liquid membrane separation. As a result of fouling, permeate production is reduced because of the continued deposition of macromolecules, particles, gels, and/or colloids on the membrane rejection surface, which can block and clog the membrane pore [2]–[4]. Membrane fouling can cause systematic adverse effects like increased operational costs and decreased system efficiency [5].

Cleaning methodologies and protocols have been developed to mitigate membrane fouling. Membrane cleaning aims to restore pure solvent flux of a membrane by removing foulants while preserving membrane integrity [6]. Physical membrane cleaning uses shear forces generated during flow to remove weakly-adhered foulants, including, forward-washing, reverse-washing, and back-washing [7]. However most hydraulic cleaning methods require a period of system shutdown, and therefore, reduce the production rate. Moreso, fouling is allowed to progress until a level of inefficiency is reached, where it is not actively addressed in the separation process. Postponing membrane cleaning provides opportunity for reversible foulants to become strongly adhered to one another, becoming a more challenging foulant to remove [8]. Consequently, chemical membrane cleaning techniques are used to remove these strongly adhered, irreversible foulants. However the use of harsh chemical reagents can not only cause damage to the polymeric membranes (even when used with mild concentrations) [9], but also raises environmental concerns [10].

Motivated by the limitations associated with current methods, new physical membrane cleaning techniques have been developed that focus on enhancing mass transport at the membrane interface, e.g. incorporating scouring particles into feed solution [11], vibrating the

membrane during active separation [12], and generation of discrete, turbulent vortices by imposing oscillations and pulsations into feed flow [13].

In contrast to membrane cleaning techniques, some researchers have shifted attention to alternative antifouling techniques by modifying the surface of a membrane [14]. In consideration of this, both chemical and topological properties of membrane surfaces will dictate the interactions between membrane and potential foulants [15], [16]. Topological modifications of membrane surfaces, such as surface patterning, have been experimentally demonstrated to show that physical sub-micron features can generate localized turbulence that reduces the propensity of membrane fouling in crossflow conditions [17], [18]. Despite the enhanced membrane lifetime, surface patterned membranes do not actively address membrane fouling in real time and only offer passive antifouling benefits while separation occurs. Notably, oscillating gas bubbles have shown great promise for generating in-situ turbulence and can be remotely actuated from a wide array of sources like acoustics [19]–[21], electrical [22], and mechanical vibrations [23]. When a bubble is acoustically actuated, oscillations of the gas-liquid-interface (GLI) generate steady streaming effects, which will be referred to as acoustic microstreaming [24], [25]. The behavior of acoustic microstreaming microbubble is well studied in the microfluidics field to achieve mixing [19], pumping [20], particle manipulation [26], and even drug delivery [27], [28]. Even in different viscous media that are relevant to bio-separation processes [29], trapped bubbles have been shown to generate steady streaming effects. In spite of this, the acoustic microstreaming bubbles demonstrated in microfluidic applications primarily exhibit 2dimensional (2D) streaming effects due to channel confinement where z-axis heights are much smaller than x-axis and y-axis channel features.

The steady streaming effects generated by oscillating microbubbles can be potentially harnessed for mitigating membrane fouling, which requires 3-dimensional (3D) fluid streaming under bulk membrane separation conditions. While sharp-tip acoustic streaming microstructures have been previously demonstrated to remove a formed cake layer on a membrane surface, the streaming effects also predominantly act in 2D and only offer fluid disturbances over a few hundred microns [30]. To date, some researchers have developed entrapment techniques to preserve the hemispherical shape of bubbles to achieve 3D streaming effects. Popularized methods involve additive manufacturing (i.e., 3D printing) [31], [32] or subtractive manufacturing (e.g., laser ablation) [33], [34] to fabricate void space needed for gas entrapment. While previous studies have identified that acoustic response of trapped bubble can be enhanced when minimizing orifice diameter and increasing bubble length [34], [35], little knowledge is available when examining the effects of increased bubble volume of a structure. Furthermore, there are no known published reports on the acoustic microstreaming behaviors of hemispherical microbubbles under hydrostatic pressure or crossflow conditions, as commonly used in membrane separation processes.

In this paper, we investigate how 3D printed Helmholtz bubble-trapping-structures (BTSs) can be used to trap ambient gas for acoustic microstreaming effects in quiescent, pressurized, and crossflow conditions. The "Helmholtz" nickname chosen for BTSs was inspired by the resemblance towards Helmholtz resonators, which are also known for oscillating trapped air within a cavity. The frequency dependence of bubble dynamics is analyzed and correlated with bulk fluid streaming behavior without the presence of fluid flow. Stability of trapped bubbles are also examined which indicates a wetting transition that increases the amplitude of oscillation for enhanced turbulent streaming effects. Hemispherical bubbles are then separately

evaluated to perform acoustic microstreaming under hydrostatic pressure and crossflow. The results provide clear guidance and insights for potentially harnessing 3D acoustic microstreaming effects of entrapped bubbles for on-demand fouling mitigation in different membrane systems.

2. Materials and Methods

2.1 3D printing of bubble-trapping-structures and testing devices

Helmholtz BTSs were 3D printed with a commercial liquid crystal display (LCD) vat photo-polymerization printer (Anycubic Photon M3, Anycubic, China) with an elastomeric resin (SuperFlex, 3DMaterials, Republic of Korea). Standard Tesselation Language (STL) files for the printed structures are found in the **Supplementary Information**. Parts were sliced 50 µm thick, with 6 burn-in layers printed for 30 s and subsequent layers printed for 2.25 s. The computer aided design (CAD) model can be seen below in **Fig. 1.A**. Each individual structure stands at 3 mm tall and spans 2 mm in diameter. To increase printing throughput, evenly spaced 2 × 5 structure arrays were printed onto a 1 mm thick substrate. Each structure exhibits a hollow cylindrical cavity at the tip which connects to an internal spherical cavity for enhanced volume capture of ambient gas (**Fig. 1.A-C**). Once a print was completed, BTS arrays were detached from the build plate and immersed in an isopropanol (IPA) bath for 40 minutes. Following this step, finalized structure arrays were once again immersed in IPA and placed under vacuum for 15 minutes to fully remove any unpolymerized monomer from within the internal cavity.

The devices for visualizing and quantifying acoustic microstreaming behaviors of the BTSs were also fabricated using 3D printing. A negative mold was 3D printed for a single channel housing using a large format LCD vat-polymerization printer (AnyCubic Photon M3 Max) with the following resin (Water Washable 3D Print Resin, Anycubic, China). The 45 mm

long flow channel (W = 10 mm, H = 2.5 mm) was designed for bulk volumetric fluid flow. Finalized prints underwent the same post process as described above. Once uncured resin was removed with IPA, printed molds were further cured with ultraviolet light (OmniCure S2000, Excelitas Technologies, USA) for 15 minutes at 14 mW/cm² at room temperature [36].

Following this, a 10:1 weight ratio solution of polydimethylsiloxane (PDMS) (Sylgard 184, Dow, USA) was thoroughly mixed for 5 minutes and degassed before pouring into the mold. The filled mold was degassed again, cured for 1 hour at 60 °C, and allowed to air cool before de-molding. The inlet and outlet of each device were punched-out with a surgical punch biopsy. Both the PDMS housing and 1 mm thick glass slide (Cat. No. 12550C, Fisher Scientific, USA) were subjected to 1 minute of oxygen plasma treatment (PDC-001, Harrick Plasma, USA) to promote strong bonding between both materials. Uncured PDMS solution (10:1) was then applied to the base of the cured channel housing to act as a bonding mortar. Prior to housingsubstrate-attachment, a single BTS was cut from the parent array and adhered to the glass slide with epoxy (ClearWeldTM Syringe, J-B Weld, USA) to avoid hydrophilic functionalization of the gas entrapment geometry. The single structure was adhered to the glass slide on its side to visualize the dynamics of the GLI and the lateral streaming profile generated. The liquid PDMS adhesive was allowed to cure overnight at room temperature to create a watertight seal between glass slide and channel housing. The device was then allowed to cure at 60 °C on a hotplate overnight to fully cure the PDMS and improve bonding strength. A piezoelectric transducer (PZT) (Model No. 7BB-27-4, Murata Electronics, Japan) with a resonant frequency of 4.6 kHz ± $0.5~\mathrm{kHz}$ was adhered adjacent to the channel housing with a thin layer of epoxy (ClearWeldTM Syringe, J-B Weld, USA) (Fig. 1.D). An example of streaming profile of the acoustically excited BTS is shown in **Fig. 1.E**.

2.2 Characterization of acoustic streaming of BTS

Gas (air) is trapped within the 3D printed BTS when a fluid is injected into the inlet of the PDMS device, and the orifice becomes submerged. To minimize variability in bubble wetting due to inertial effects during fluid injection, a single 3 mL syringe (SKU: 309657, BD Biosciences, USA) being driven at 100 μL/min with a syringe pump (Model no. Fusion 200, Chemyx Inc., TX, USA) was implemented into the experimental protocol. Both fluids used in this work, deionized (DI) water and 5 μm polystyrene particle suspension (Cat. No. PS06001, Bangs Laboratories Inc., USA), were stored at room temperature to maintain both liquid and trapped air in thermodynamic equilibrium. The 5 μm polystyrene particles were used as tracer particles for visualization of the induced acoustic microstreaming hydrodynamics. They are the smallest diameter particles that allow for accurate particle image velocimetry (PIV) measurements at both high and low magnification.

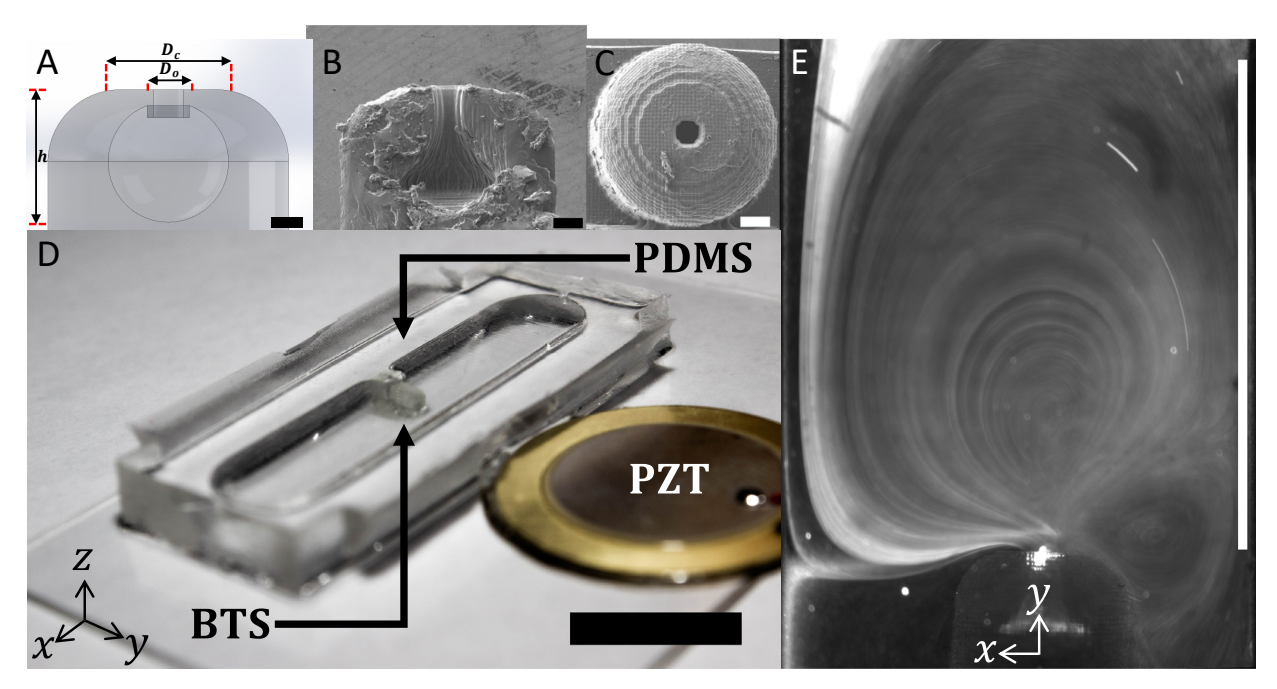


Fig. 1. Helmholtz bubble-trapping-structure and experimental flow device. (A) CAD model cross sectional area image of 3D printed Helmholtz structure (scale bar = $300 \mu m$). SEM images of (B) cross sectional view (scale bar = $300 \mu m$) and (C) Top-down view of the BTS structure

(scale bar = $300 \,\mu\text{m}$). (D) PDMS flow device used to study the BTS steaming behaviors (scale bar = $20 \,\text{mm}$). (E) An example of long exposure fluorescent image of acoustic microstreaming effects generated by the BTS (scale bar = $4.0 \,\text{mm}$).

To create an acoustic field for bubble excitation, a sinusoidal signal was generated by an arbitrary waveform generator (3600A Series, Keysight, USA) and amplified 5 times by an external output amplifier (33502A, Keysight, USA) to drive piezoelectric actuation. An applied voltage of 30 V, the limit of the transducer, was chosen to generate the most intense, turbulent, and laterally extending streaming profiles.

The acoustic microstreaming experiments were performed on an inverted microscope (Ti2-U, Nikon, Japan) equipped with a high-performance video camera (FASTCAM SA4, Photron, Japan). Given the large diameter of the GLI and small working distance of a microscope objective, a unique scaling approach was adopted to estimate print fidelity of BTS geometries and the respective microstreaming effects produced from each structure. To determine a representative pixel-to-distance scale factor, spatial dimensions of completed BTSs were resolved by referencing known lengths of finalized prints. More details can be found in the **Supplementary Information**.

PIV is implemented to characterize the forced acoustic response of a bubble and quantify the acoustic microstreaming effects. For capturing large-scale microstreaming profiles in the lateral plane of a structure, a framerate of 10 kHz was chosen to quantify the finite changes in trajectory a particle experiences while moving across millimeter distances. Additionally, 10 kHz framerate was used to image oscillation behaviors of the GLI during frequency sweep characterization. Amplitude of oscillation is measured by hand on ImageJ and related to the maximum streaming velocity (v_{ω}) at the given frequency. Given the 3D toroidal streaming effects produced from the oscillations of the GLI, only velocities in the XY plane are reported, as

illustrated in **Fig. 1.E**. For bubble dynamics characterization, a framerate of 50 kHz was chosen to fully capture differences in bubble oscillations, which adheres to the Nyquist Sampling Theorem for the considered range of acoustic driving frequencies (100 Hz to 20 kHz).

To characterize acoustic microstreaming BTSs under conditions akin to membrane separation, hydrostatic pressure and crossflow experiments were carried out. The effects of pressure on microstreaming bubble were explored by imposing hydrostatic pressures on a BTS while performing microstreaming. A syringe pump was used to inject a 5 μ m particle suspension into the flow device and was completed once the outlet tubing had become full. Different hydrostatic pressures ($P_{hydrostatic} = \rho g h_l$) were exploited by raising the end of the tubing to different heights, where ρ is the density of the liquid, g is the acceleration due to gravity, and h_l is the height of the liquid. The ability of the BTSs to generate turbulent effects in crossflow was evaluated by increasing the volumetric flow rate of the syringe pump and studying the microstreaming effects produced. The bulk fluid streaming response is captured at each increase of crossflow velocity (v_{cf}) until microstreaming effects are dominated.

3. Results and Discussion

3.1 Design of the 3D printed Helmholtz structure

It is known that the physical attributes of gas trapping geometries play a pivotal role in the acoustic microstreaming behavior of a bubble [33], [37]–[40]. The 3D printed Helmholtz BTS design consists of a cylindrical structure with a hollow cavity feature positioned at the rounded tip (**Fig. 1. A-C**). This structure design is inspired by the double re-entry hollow cavity used in acoustically controlled swimming microrobots [41], [42], where improved stability of the swimmer was achieved due to the omniphobicity associated with the structure. For the targeted applications in aqueous media seen in most membrane processes, a hydrophobic resin

was chosen (water contact angle = 96°, **Fig. S1**). With such a combination of structural design and material chemistry, the BTS displayed stability over 48 hours without any further surface treatments.

In our 3D printing CAD model, the geometry of the BTS includes an orifice diameter (D_0) of 250 µm, an internal cavity diameter (D_c) of 1000 µm, and a total bubble height of 1100 µm (h, the distance from the orifice opening to the bottom of the cavity). These critical dimensions for the BTS are much smaller than the acoustic excitation wavelengths considered $(\lambda(4.0 \text{ kHz}) = 375 \text{ mm} \text{ and } \lambda(7.0 \text{ kHz}) = 214.3 \text{ mm})$, which allows the GLI created by the BTS to respond strongly to acoustic frequencies [43]. Note that BTSs with smaller feature sizes, such as the swimming microrobots fabricated by the two-photon lithography [32], [42], [44], can produce intense streaming at higher frequencies towards ultrasound regimes, which often cause damages to both bioproducts and membranes used in the bio-separations [45]. Nevertheless, the accuracy of the 3D printed Helmholtz structure, compared with the CAD design, appears to be within 1 % difference along the vertical printing dimension (h) and 16.5 % to 20.4 % difference along the horizontal printing direction (D_o and D_c , respectively), as listed in **Table 1.** discrepancy in lateral and vertical printing accuracy is common to the layer-by-layer 3D printing mechanism. From SEM images, small inhomogeneities were observed on the inside of the cavity wall (Fig. 1.B). In addition, terrace-like edges were observed surrounding the orifice perimeter (Fig. 1.C), which may affect the contact line between the liquid and entrapped gas [39], which will be discussed later.

Table 1. 3D printing fidelity for Helmholtz bubble-trapping-structure

feature	CAD length (µm)	measured length (µm)	difference %
D_o	250.0	295.0	16.5
D_{c}	1000.0	814.7	20.4

h 1100.0 1089.0 1.0

3.2 Characterization of oscillating trapped bubble

When a BTS becomes submerged in an aqueous medium, gas is instantly trapped within the cavity forming a GLI at the orifice. Under acoustic excitation, the GLI is expected to oscillate harmonically to generate fluid streaming. **Figure 2.A** shows the images of the GLI oscillation captured during one period of acoustic excitation at a frequency of 4.5 kHz. A custom MATLAB routine was developed to track the image contrast associated with the GLI during active acoustic excitation. Specifically, the oscillation amplitude of the GLI, defined as the change in the length of the GLI protrusion (l_p , **Fig. 2.A**), was quantified as a function of time. **Figure 2.B** shows the time-dependent position of the GLI for roughly 100 oscillation cycles. Fast Fourier transformation analysis of the time-dependent position data reveals that the GLI oscillates at the driving frequency or the 1st theoretical harmonic (**Fig. 2.C**). The analysis confirms that the GLI radially compresses/expands harmonically in response to the oscillatory pressure field in the fluid domain.

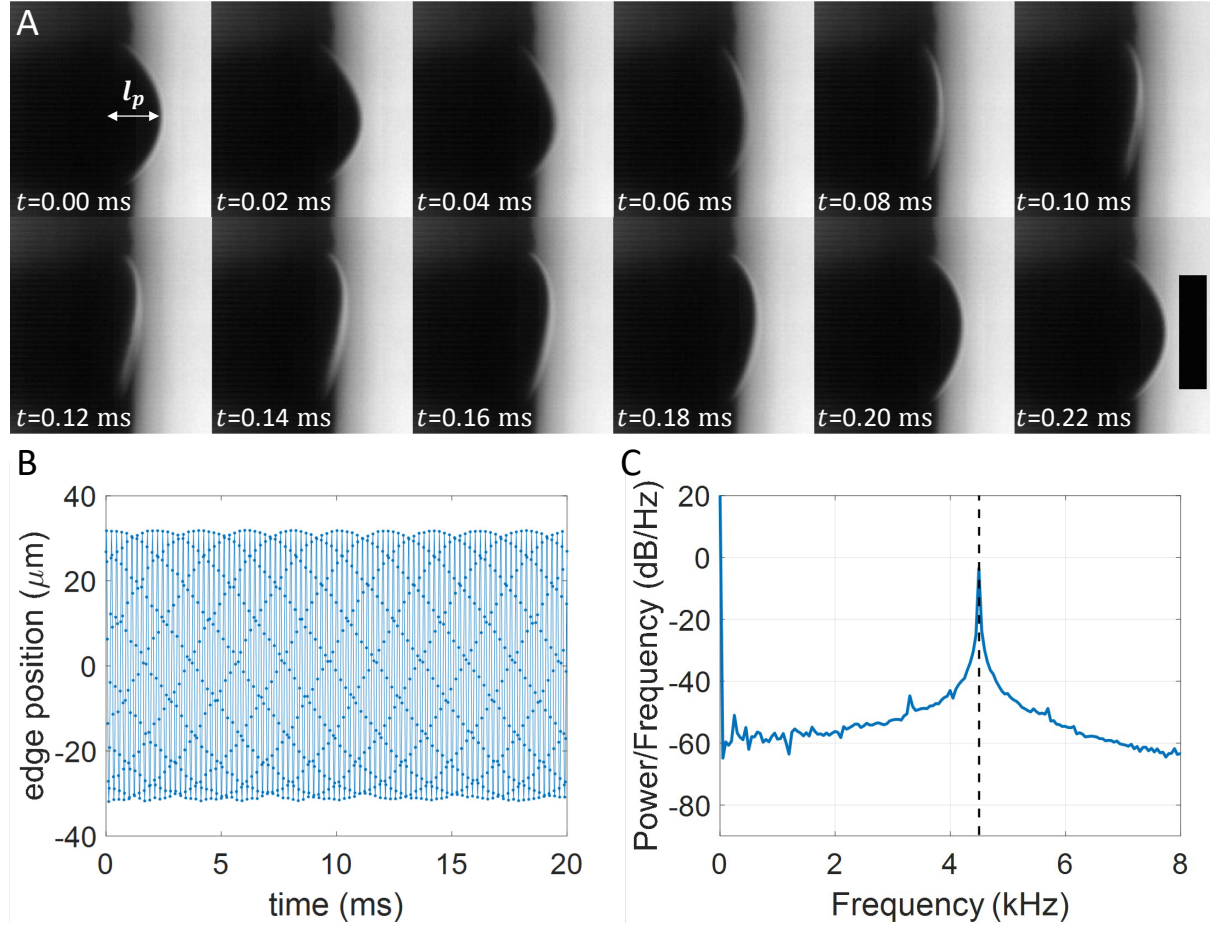


Fig. 2. Quantified bubble oscillations in DI water for an acoustic field driven at 4.5 kHz. (A) Snapshots of the GLI completing one full cycle of acoustic excitation (scale bar = 250 μ m). (B) Change of position of the GLI interface over time as it oscillates harmonically. (C) Fast Fourier transformation analysis of time-dependent position data of the GLI. The first peak perfectly matches the dotted asymptote which represents the first theoretical harmonic of the driving frequency.

3.2.2 Resonant microstreaming

The behavior of bubble oscillations, or bubble mode shapes, is mainly dependent on excitation frequency along with a variety of intrinsic properties of the gas. Mode shapes of sessile bubbles can be described by the number of nodes counted along both radial and sectoral (diameter) directions of the oscillating interface [46]. For example, the classical [0,1] "breathing" mode shape refers to a single radial node that oscillates about the pinned interface without any sectoral deformations on the GLI, as described in **Fig. 2.A**. Forcing harmonic oscillations onto

bubbles generates unique mode shapes on the GLI and are known to give rise to various microstreaming patterns [47]–[49]. To generate the most turbulent microstreaming effects, actuating bubbles at or near resonance is generally recommended because amplitude of oscillation is greatest. The geometry of the 3D printed BTSs resemble that of a gas-filled pore [39], [40], whose resonant frequency can be estimated from **Eqn. 1** below,

$$f_0 = \frac{1}{2\pi} \left[\frac{120\pi\sigma h + 15\pi\kappa P_0 a^2}{32\rho a^3 h} \right]^{0.5} (1)$$

where σ is the interfacial surface tension, ρ is the density of the liquid, h is the bubble height, κ is the polytropic index, P_0 is the gas pressure when the interface is flat, and a is the radius of the orifice (= $D_0/2$). More sophisticated models have been developed that consider further intricacies of bubble oscillations like radius of bubble curvature, wetting contact angle constraints, shape number and more [25], [50]–[52]. Despite this, the simple expression in **Eqn.** 1 developed by Miller and Nyborg [39] best describes the physical attributes of our system that takes bubble height and orifice diameter into consideration. A resonant frequency of 5.47 kHz was predicted for a Helmholtz BTS of flat and pinned interface, using $\sigma = 0.072$ N/m, $P_0 = 101325$ Pa, $\rho = 1000$ kg/m³, $\kappa = 1.0$ (assumed isothermal), $\alpha = 147.5$ µm, and $\alpha = 1089$ µm. The model assumes bubble oscillations are pinned at the three-phase contact line, which constrains the possible oscillation mode shapes of the bubble [46].

The frequency dependency of BTS microstreaming behaviors was systematically examined by visualization of the 5 µm streaming particle suspension throughout the swept frequencies of 4.0 kHz – 7.0 kHz. Note that increasing the forcing amplitude of the PZT with higher voltage is also known to enhance microstreaming intensity [22], [34], [44], which was confirmed in this study (**Fig. S2**). For the remaining experiments, the driving voltage was fixed at 30 V, the limit of the transducer.

Figure 3.A shows the maximum v_{ω} of the particles and amplitude of GLI oscillation as a function of excitation frequency. Interestingly, the system displayed multiple resonance peaks even within this relatively narrow range of frequency. This contrasts most reported microstreaming frequency spectra that typically describe a single resonant peak for the system at hand. Additionally, appreciable growth of the GLI l_p was observed throughout the frequency sweep, from an initially flat and pinned profile (Fig. 3.B) to a hemispherical profile with a larger radius of curvature (Fig. 3.C). The increase in protrusion length represents a 17 % volume growth of the original bubble, which is likely caused by the rectified diffusion of dissolved gas into the GLI due to the large pressure amplitude chosen for maximizing microstreaming effects [53].

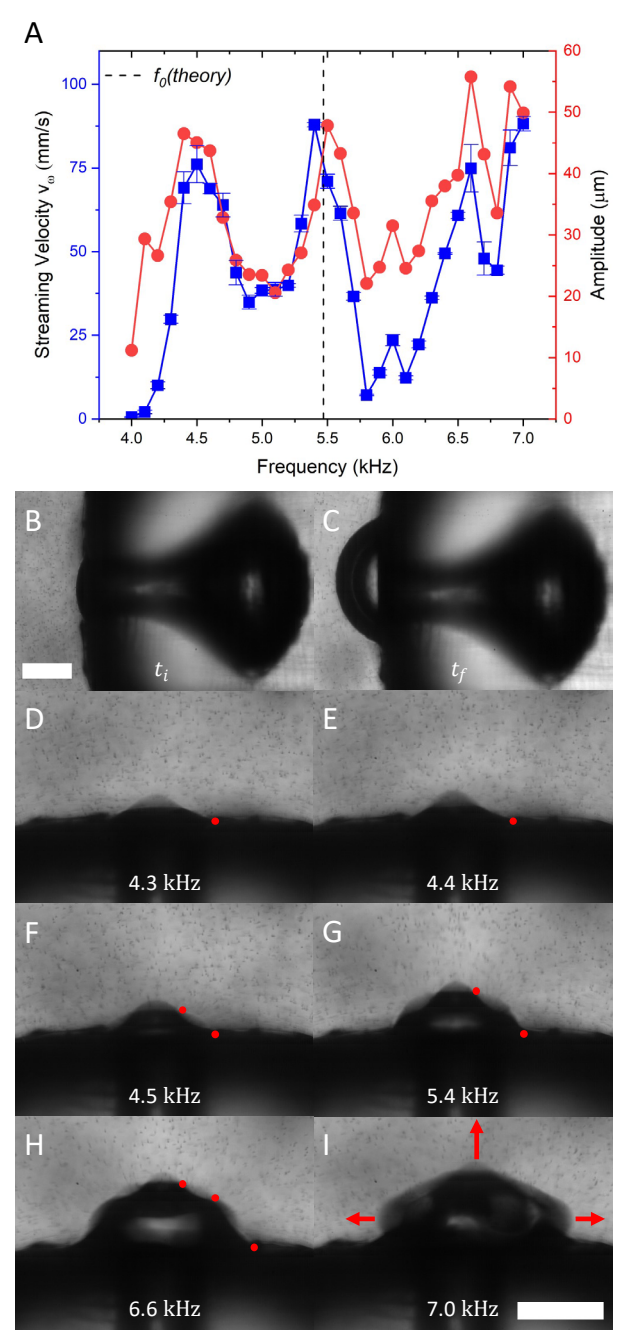


Fig. 3. Acoustic microstreaming frequency sweep and respective modes of oscillation. (A) Measured maximum particle velocity and respective amplitude of GLI oscillation versus applied driving frequency, n = 3. Theoretical resonant frequency of 5.47 kHz, estimated from Eq. (1), is indicated by the dash line. (B) and (C) are images of the GLI before and after frequency sweep (scale bar = 250 μ m). (D) and (E) are snapshots of pinned GLI performing [0,1] mode shape. (F) and (G) are snapshots of de-pinned GLI performing [0,2] mode shape with a v_{ω} of 76 mm/s and 88 mm/s, correspondingly. (H) Snapshot of de-pinned GLI performing [0,3] mode shape, reaching a v_{ω} of 75 mm/s. (I) Snapshot of de-pinned GLI performing unknown mode shape, reaching a v_{ω} of 88.2 mm/s. Additional microstreaming jets are observed at the sides of the oscillating GLI as indicated by arrows (scale bar = 250 μ m).

It has been shown that the streaming behaviors of trapped bubbles depend on the length of bubble protrusion [54]. In our case, the evolution of GLI profiles led to the complex microstreaming behaviors summarized in Fig. 3.A. At lower frequencies (between 4.0 kHz and 4.4 kHz), the pinned GLI appeared to oscillate in the [0,1] breathing mode (Fig. 3.D – 3.E). Increasing the frequency to 4.5 kHz generated the first v_{ω} peak and caused the GLI to become de-pinned from the orifice perimeter. The intense streaming effects and de-pinning of the GLI suggests that 4.5 kHz is the true resonance of the initial GLI when considering the governing assumptions in Eqn. 1. The two additional streaming peaks that were generated at higher frequencies are likely to have been actuated at sub-resonance conditions due to the increased GLI size. Despite the disagreement between theoretical resonance (5.47 kHz) and experimental resonance (4.5 kHz), the resonant frequency model still provides satisfactory abilities in identifying general locations of resonance for gas-filled pockets like the BTS.

Figure 3.F shows the sides of the bubble radially expanding outward during the gas compression stage of the oscillation, which indicates a dynamic three-phase contact line. Such depinning of GLI contact line is caused by the inertial effects that take place when microstreaming in bulk fluid media. Steady microstreaming flows are driven by the non-zero Reynolds stresses due to the inertia of the fluid mass oscillating against the GLI [55], [56]. When surface tension forces attempt to "snap" back to equilibrium position, inertial effects of fluid mass can alter the wetting state. Inertial instabilities during microstreaming are not commonly reported in microfluidic systems, where surface tension forces dominate over volumetric forces due to the smaller length scale and channel confinement. Nevertheless, de-pinning of the GLI enables the bubble to oscillate with less boundary constraints than when pinned, leading to exceptional rates of gas expansion/compression during steady oscillation. As a result, the newly

wetted bubble (**Fig. 3.G**) appeared to be performing [0,2] mode shape given the number of static nodes counted along the oscillating GLI silhouette, which gives rise to the second peak of GLI oscillation and particle streaming with a $v_{\omega} = 88$ mm/s.

Figure 3.H illustrates the enlarged bubble oscillating with the [0,3] mode shape at 6.6 kHz, which generates comparable streaming velocities as the [0,1] and [0,2] mode shapes. The frequency sweep is concluded at 7.0 kHz, which actuated the fastest microstreaming mode shape (88.2 mm/s) of the entire experiment (Fig. 3.I). Due to the de-pinning of the GLI and growth of l_p , its possible translative mode shapes emerged at 7.0 kHz due to the shifted center position of the hemispherical bubble. Accurately defining the 7.0 kHz mode shape is not possible like previously due to the chaotic asymmetric profile of the GLI. The nearly hemispherical interface radially oscillates with new modal symmetries. Interestingly, the 7.0 kHz mode shape is the only oscillation pattern that generates steady lateral streaming effects on the sides of the interface instead of the recirculatory flow observed at lower frequencies. Experimental videos of highlighted mode shapes mentioned above can be found in the Supplementary Information.

In our experiments, modestly different initial bubble protrusion lengths were observed even for the same BTS. Such differences can affect the generated streaming effects for bubbles of identical cavity [35]. The frequency responses of the streaming behaviors of two other experiments are shown in **Fig. S3** and **Fig. S4**. Similar to **Fig. 3**, both GLIs showed growth of bubble protrusions throughout the experiment and evolution of mode shapes, which resulted in multiple peaks of resonance streaming within the same frequency range, with peak streaming velocities as great as 100 mm/s. However, the shape (specific position of the peaks) of the streaming curves differ, which highlights the sensitivity of the GLI. In consideration of this

sensitivity, all future resonant frequency determination was simply found by choosing the qualitative streaming maxima during frequency sweep.

Such evolving GLI profiles pose challenges for maintaining microstreaming under optimum resonance conditions. Figure 4.A shows evolution of the particle velocity as a function of distance from bubble interface and duration of excitation. A drive frequency of 4.5 kHz was chosen based on the qualitative streaming intensity observed at that frequency. Notably, v_{ω} was measured to be 125 mm/s, which produced the most intense streaming effects presented in this study. A region of interest (ROI) (Fig. S5) up to 4 mm from the GLI was defined to capture the strongest streaming effects that occur along the axisymmetric streaming profile. beginning, the interface height remained level with the structure orifice (Fig. 4.B), which appeared to oscillate with a [0,2] mode shape where microstreaming velocities were maximized. The particle velocity rapidly decayed as a function of distance away from the GLI interface, consistent with microstreaming literature reports [48], [57]. The maximum v_{ω} decreased to less than 80 mm/s after 10 minutes and to 30 mm/s after 30 minutes of continuous acoustic excitation, correspondingly. Such an appreciable reduction in v_{ω} is attributed to the evolution of GLI during the experiment. At the end of the experiment, the GLI had grown beyond the boundaries of the structure orifice (Fig. 4.C). Accompanying the growth of the bubble protrusion, the resonance frequency may have shifted from 4.5 kHz during the continuous application of the acoustic field.

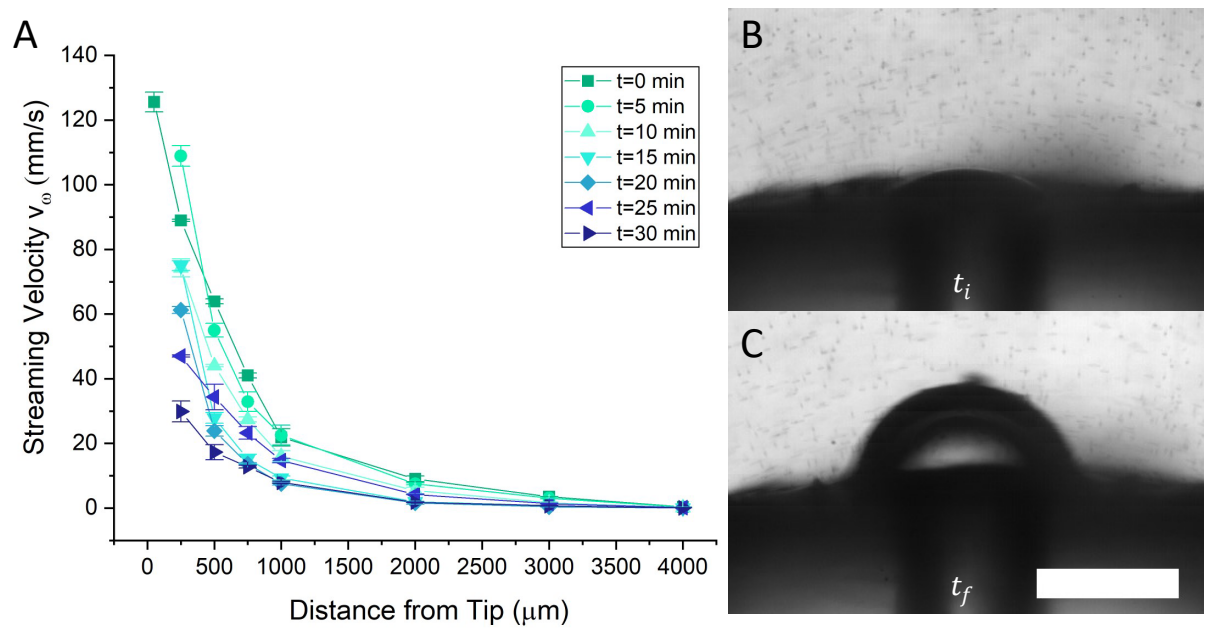


Fig. 4. Temporal microstreaming at resonant conditions. (A) Maximum particle streaming velocities along 4 mm streaming distance in lateral plane of the BTS, taken at different times during the 30 minute continuous acoustic field excited at 4.5 kHz, n = 3. (B) Initial GLI shape after resonant frequency was qualitatively determined. (C) Final GLI shape after experiment completed showing bubble volume growth (scale bar = 250 μ m).

3.3 Acoustic microstreaming in non-quiescent conditions

3.3.1 Pressurized microstreaming

To potentially apply the BTS for effective fouling mitigation in membrane processes, the effects of hydrostatic pressure and crossflow on the microstreaming behaviors need to be characterized. Hydraulic pressure is used both to drive feed flow across the feed channel (pressure drop) and permeate through the membrane (transmembrane pressure). **Figure 5** displays particle velocity maps under different hydrostatic pressures created by different head heights of the outlet tubing. Each particle velocity map shows the streaming pattern, intensity, and angle of trajectory across the lateral plane of the BTS under a 5.5 kHz acoustic field excitation, which was determined to provide the best streaming effects.

The velocity map pictured in **Fig. 5.A** illustrates the streaming profile when oscillating at resonance without hydrostatic pressure. Large lateral streaming velocities were observed in the

front of the bubble protrusion (59.6 mm/s) while recirculation flow occurred on both sides. Increasing $P_{hydrostatic}$ to 2.96 kPa (**Fig. 5.B**) and to 6.0 kPa (**Fig. 5.C**) did not alter the overall steaming pattern significantly, but correspondingly reduced the maximum v_{ω} to 36.1 mm/s and to 25.7 mm/s, respectively. At $P_{hydrostatic} = 9.0$ kPa, the microstreaming of particles occurred only within a 500 μ m vicinity of the GLI (**Fig. 5.D**).

Increasing hydrostatic pressure steadily compressed the trapped air within the BTS shown in **Fig. 5.E**, causing the bubble protrusion length to reduce from 210 μ m to 57 μ m. When hydrostatic pressure load was removed from the flow device, the majority of the original bubble protrusion length was restored. The observations above suggest that $P_{hydrostatic}$ decreases the GLI profile which results in the shift of its resonance frequency, and therefore, diminished microstreaming effects. Note, an additional frequency sweep was conducted on the compressed GLI at the original drive frequency but generated insignificant streaming effects when re-cycling through the acoustic frequency regime.

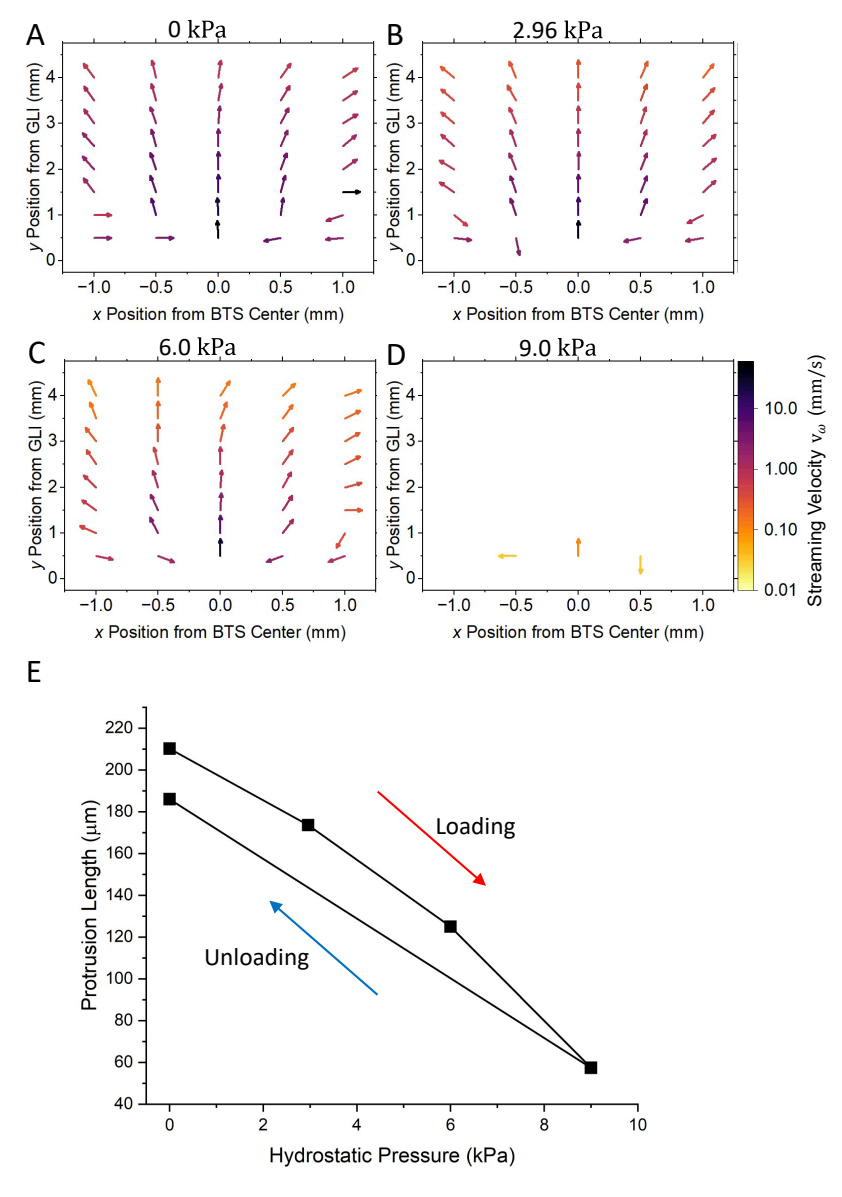


Fig. 5. Effects of hydrostatic pressure on microstreaming effects. Microstreaming velocity maps driven at 5.5 kHz of different $P_{hydrostatic}$ loads imposed onto the flow device: (A) 0 kPa, (B) 2.96 kPa, (C) 6.0 kPa, (D) 9.0 kPa. The color map scale bar = $\log 10(v_{\omega})$. (E) Changes of bubble protrusion length (l_p) when loading/unloading hydrostatic pressure.

3.3.2 Crossflow microstreaming

To date, most experimental work on 3D printed BTSs have been carried out under static conditions [42], [44], [58], whereas no published studies have examined the effects of bulk fluid crossflow. **Figure 6** shows three microstreaming velocity maps obtained under an acoustic excitation at 6.5 kHz under different crossflow conditions: i) static condition with no crossflow

(**Fig. 6.A**), ii) a v_{cf} of 0.093 mm/s (**Fig. 6.B**), and iii) a v_{cf} of 0.20 mm/s (**Fig. 6.C**), which was the largest crossflow velocity before microstreaming effects were reduced to within 1 mm away from the GLI. Note that the reported v_{cf} values within the channel are averages, assuming a parabolic flow profile in the PDMS flow channel.

Under no-crossflow condition (Fig. 6.A), the BTS displayed maximum v_{ω} of 28.4 mm/s which was significantly lower than the values shown in Fig. 3. The discrepancy was attributed to the initial bubble wetting state and GLI profile obtained for the crossflow experiments. Nevertheless, the GLI still generated an intense axial symmetric streaming profile where particle trajectories began to disperse at distance y = 3.5 mm away from the GLI. The v_{ω} rapidly decreases as a function of distance away from the GLI, similar to that shown in Fig. 3. At a v_{cf} of 0.093 mm/s (Fig. 6.B), the streaming profile was still symmetrical but the particles furthest from the GLI were seen to be taken downstream by the crossflow. The particles overcome by crossflow traveled marginally faster than imposed v_{cf} (~0.2 mm/s), causing the streaming profile to be slightly shifted in the direction of flow. Accordingly, maximum v_{ω} was reduced to 20.1 mm/s. Acoustic microstreaming effects generated by the BTS were nearly overcome by a v_{cf} of 0.20 mm/s (Fig. 6.C), as the maximum v_{ω} was diminished to 6.18 mm/s and the effective streaming profile was limited to less than 1 mm away from the GLI. Particles taken downstream were measured to travel at comparable speeds as the imposed crossflow velocity, illustrating the competition of energies between streaming particles and crossflow rates.

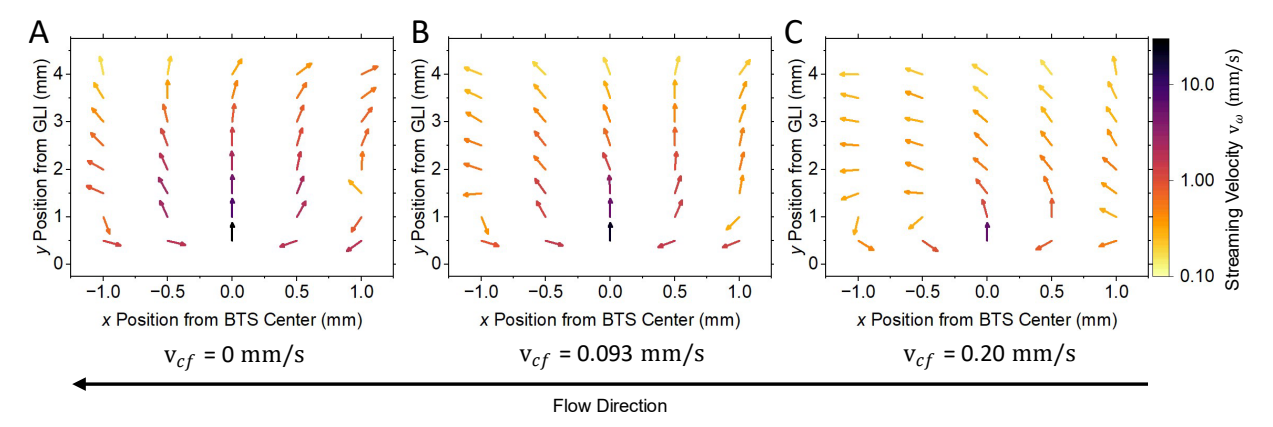


Fig. 6. Acoustic microstreaming resiliency in crossflow conditions. (A) Velocity map of microstreaming bubble at resonance in static flow conditions driven at 6.5 kHz. (B) Velocity map of microstreaming bubble with a v_{cf} of 0.093 mm/s. Microstreaming patterns are beginning to be overcome by crossflow effects. (C) Velocity map of microstreaming bubble with a v_{cf} of 0.20 mm/s. Microstreaming patterns are overcome by crossflow effects. The color map scale bar = $log10(v_{\omega})$.

Prior studies of 2D microstreaming bubbles have demonstrated notable microstreaming resiliency in higher crossflow velocities (1.33 mm/s [47], 1.34 mm/s [59], and 5.55 mm/s [60]) than reported in this work. Compared to 2D microstreaming bubbles, the acoustic microstreaming effects for 3D printed BTS are more easily diminished in crossflow conditions due to lessened boundary constraints. The hemispherical GLI of Helmholtz BTS only occupies a portion of the channel height and is only constrained by the wetting perimeter of the orifice structure. As a result, fluid flow is forced around the hemispherical GLI which introduces additional shear stress contributions that can negatively impact microstreaming effects due to GLI deformations. On the other hand, the GLI of 2D bubble is physically constrained to the entire channel height due to the sandwiching configuration most microfluidic devices are constructed in. In turn, microstreaming effects are more prominently observed under crossflow because the amplitudes of 2D bubbles uniformly perturb the entire parabolic flow profile with each oscillation cycle. Albeit the differences in velocity magnitude, 2D microstreaming bubbles

are recognized to have a similar range of lateral streaming effects in crossflow that are observed to also persist only a few hundred microns beyond the oscillating GLI.

Conclusion

In this work, the acoustic microstreaming behavior of 3D printed Helmholtz BTSs are studied for active membrane anti-fouling in aqueous media. Through a combination of structural design inspired by acoustically controlled microrobots and material chemistry, BTSs are demonstrated to display gas stability for over 48 hours without additional surface treatments. Experimentally, the influence of excitation frequency, hydrostatic pressure, and crossflow conditions on microstreaming BTSs are studied. High intensity, lateral streaming profiles are generated from a wide variety of bubble mode shapes for both pinned and de-pinned wetting states. Notably, this study reveals the sensitivity of microstreaming bubbles to external factors such as hydrostatic pressure and crossflow. Large bulk fluid disturbances were obtained until a hydrostatic pressure load of 9.0 kPa, which impeded streaming effects to a 500 µm range of the GLI. The findings also highlight the differences in microstreaming resiliency between 3D printed BTS and 2D microstreaming bubbles, indicating the need for further exploration and optimization to harness the full potential of BTSs in crossflow environments. In the future, efforts will be made to fine tune the microstreaming stability of Helmholtz BTS for reliable and continuous operation within a flat sheet membrane separation module. In perspective, Helmholtz structures can be orientated towards the surface of the membrane by fixing structures atop the feed channel ceiling. Significant research efforts are needed to achieve optimum antifouling efficiency by optimizing the distance between membrane surface and Helmholtz structure, as well as the design of Helmholtz structures (length, number and spatial configurations).

Acknowledgements

We acknowledge the support from the National Science Foundation (NSF) Industry/University Cooperative Research Center for Membrane Science, Engineering and Technology (MAST) at the University of Colorado Boulder (UCB, award number, IIP 1624602). KF acknowledges the support of AMTA-NWRI fellowship. Publication of the National Institute of Standards and Technology (NIST), an agency of the US government, is not subject to copyright. Commercial equipment, instruments, or materials are identified only in order to adequately specify certain procedures. In no case does such identification imply recommendation or endorsement by NIST, nor does it imply that the products identified are necessarily the best available for the purpose.

References

- [1] P. Bacchin, P. Aimar, and R. Field, "Critical and sustainable fluxes: Theory, experiments and applications," *J. Membr. Sci.*, vol. 281, no. 1–2, pp. 42–69, Sep. 2006, doi: 10.1016/j.memsci.2006.04.014.
- [2] A. Cassano, M. Marchio, and E. Drioli, "Clarification of blood orange juice by ultrafiltration: analyses of operating parameters, membrane fouling and juice quality," *Desalination*, vol. 212, no. 1, pp. 15–27, Jun. 2007, doi: 10.1016/j.desal.2006.08.013.
- [3] Q. She, R. Wang, A. G. Fane, and C. Y. Tang, "Membrane fouling in osmotically driven membrane processes: A review," *J. Membr. Sci.*, vol. 499, pp. 201–233, Feb. 2016.
- [4] P. Le-Clech, V. Chen, and T. A. G. Fane, "Fouling in membrane bioreactors used in wastewater treatment," *J. Membr. Sci.*, vol. 284, no. 1–2, pp. 17–53, Nov. 2006.
- [5] N. AlSawaftah, W. Abuwatfa, N. Darwish, and G. A. Husseini, "A Review on Membrane Biofouling: Prediction, Characterization, and Mitigation," *Membranes*, vol. 12, no. 12, p. 1271, Dec. 2022, doi: 10.3390/membranes12121271.
- [6] G. Aysegul, J. Hruza, and F. Yalcinkaya, "Fouling and Chemical Cleaning of Microfiltration Membranes: A Mini-Review," *Polymers*, vol. 13, p. 846, 2021.
- [7] Z. Wang, J. Ma, C. Y. Tang, K. Kimura, Q. Wang, and X. Han, "Membrane cleaning in membrane bioreactors: A review," *J. Membr. Sci.*, vol. 468, pp. 276–307, Oct. 2014.
- [8] H. J. Tanudjaja *et al.*, "A review of membrane fouling by proteins in ultrafiltration and microfiltration," *J. Water Process Eng.*, vol. 50, p. 103294, Dec. 2022, doi: 10.1016/j.jwpe.2022.103294.
- [9] B. Malczewska and A. Żak, "Structural Changes and Operational Deterioration of the Uf Polyethersulfone (Pes) Membrane Due to Chemical Cleaning," *Sci. Rep.*, vol. 9, no. 1, p. 422, Dec. 2019.
- [10] S. Wang, J. W. Chew, and Y. Liu, "An environmentally sustainable approach for online chemical cleaning of MBR with activated peroxymonosulfate," *J. Membr. Sci.*, vol. 600, p. 117872, Apr. 2020, doi: 10.1016/j.memsci.2020.117872.
- [11] Z. Zhong, W. Xing, X. Liu, W. Jin, and N. Xu, "Fouling and regeneration of ceramic membranes used in recovering titanium silicalite-1 catalysts," *J. Membr. Sci.*, vol. 301, no. 1–2, pp. 67–75, Sep. 2007, doi: 10.1016/j.memsci.2007.05.036.
- [12] S. Beier, M. Guerra, A. Garde, and G. Jonsson, "Dynamic microfiltration with a vibrating hollow fiber membrane module: Filtration of yeast suspensions," *J. Membr. Sci.*, vol. 281, no. 1–2, pp. 281–287, Sep. 2006, doi: 10.1016/j.memsci.2006.03.051.
- [13] X. Ni, M. R. Mackley, A. P. Harvey, P. Stonestreet, M. H. I. Baird, and N. V. R. Rao, "MIXING THROUGH OSCILLATIONS AND PULSATIONSĐA GUIDE TO ACHIEVING PROCESS ENHANCEMENTS IN THE CHEMICAL AND PROCESS INDUSTRIES," vol. 81, 2003.
- [14] O. Heinz, M. Aghajani, A. R. Greenberg, and Y. Ding, "Surface-patterning of polymeric membranes: fabrication and performance," *Curr. Opin. Chem. Eng.*, vol. 20, pp. 1–12, 2018.
- [15] M. Rickman *et al.*, "Fractionation and flux decline studies of surface-patterned nanofiltration membranes using NaCl-glycerol-BSA solutions," *J. Membr. Sci.*, vol. 527, pp. 102–110, Apr. 2017, doi: 10.1016/j.memsci.2017.01.007.
- [16] S. H. Maruf *et al.*, "Influence of sub-micron surface patterns on the deposition of model proteins during active filtration," *J. Membr. Sci.*, vol. 444, pp. 420–428, Oct. 2013, doi: 10.1016/j.memsci.2013.05.060.
- [17] S. H. Maruf, L. Wang, A. R. Greenberg, J. Pellegrino, and Y. Ding, "Use of nanoimprinted surface patterns to mitigate colloidal deposition on ultrafiltration membranes," *J. Membr. Sci.*, vol. 428, pp. 598–607, Feb. 2013, doi: 10.1016/j.memsci.2012.10.059.

- [18] S. H. Maruf, A. R. Greenberg, J. Pellegrino, and Y. Ding, "Critical flux of surface-patterned ultrafiltration membranes during cross-flow filtration of colloidal particles," *J. Membr. Sci.*, vol. 471, pp. 65–71, Dec. 2014.
- [19] D. Ahmed, X. Mao, J. Shi, B. K. Juluri, and T. J. Huang, "A millisecond micromixer via single-bubble-based acoustic streaming," *Lab. Chip*, vol. 9, no. 18, p. 2738, 2009, doi: 10.1039/b903687c.
- [20] Y. Gao, M. Wu, Y. Lin, W. Zhao, and J. Xu, "Acoustic bubble-based bidirectional micropump," *Microfluid. Nanofluidics*, vol. 24, no. 4, p. 29, Apr. 2020, doi: 10.1007/s10404-020-02334-6.
- [21] Y. Gao, M. Wu, B. I. Gaynes, R. S. Dieter, and J. Xu, "Study of ultrasound thrombolysis using acoustic bubbles in a microfluidic device," *Lab. Chip*, vol. 21, no. 19, pp. 3707–3714, 2021.
- [22] S. H. Ko, S. J. Lee, and K. H. Kang, "A synthetic jet produced by electrowetting-driven bubble oscillations in aqueous solution," *Appl. Phys. Lett.*, vol. 94, no. 19, p. 194102, May 2009, doi: 10.1063/1.3123165.
- [23] J. Vejražka, M. Zedníková, P. Stanovsky, M. Ruzicka, and J. Drahoš, "Bubbling Controlled by Needle Movement," *Fluid Dyn. Res.*, vol. 40, pp. 521–533, Jul. 2008, doi: 10.1016/j.fluiddyn.2007.12.008.
- [24] N. Riley, "Steady Streaming," *Annu. Rev. Fluid Mech.*, vol. 33, no. 1, pp. 43–65, 2001, doi: 10.1146/annurev.fluid.33.1.43.
- [25] A. A. Doinikov, S. Cleve, G. Regnault, C. Mauger, and C. Inserra, "Acoustic microstreaming produced by nonspherical oscillations of a gas bubble. I. Case of modes 0 and m," *Phys. Rev. E*, vol. 100, no. 3, p. 033104, Sep. 2019, doi: 10.1103/PhysRevE.100.033104.
- [26] L. Sun, T. Lehnert, S. Li, and M. A. M. Gijs, "Bubble-enhanced ultrasonic microfluidic chip for rapid DNA fragmentation," *Lab. Chip*, vol. 22, no. 3, pp. 560–572, 2022, doi: 10.1039/D1LC00933H.
- [27] M. Aghaamoo *et al.*, "High-Throughput and Dosage-Controlled Intracellular Delivery of Large Cargos by an Acoustic-Electric Micro-Vortices Platform," *Adv. Sci.*, vol. 9, no. 1, p. 2102021, 2022, doi: 10.1002/advs.202102021.
- [28] P. Marmottant and S. Hilgenfeldt, "Controlled vesicle deformation and lysis by single oscillating bubbles," *Nature*, vol. 423, no. 6936, Art. no. 6936, May 2003, doi: 10.1038/nature01613.
- [29] A. J. Conde, I. Keraite, A. E. Ongaro, and M. Kersaudy-Kerhoas, "Versatile hybrid acoustic micromixer with demonstration of circulating cell-free DNA extraction from sub-ml plasma samples," *Lab. Chip*, vol. 20, no. 4, pp. 741–748, 2020, doi: 10.1039/C9LC01130G.
- [30] K. Fung, Y. Li, S. Fan, A. K. Fajrial, Y. Ding, and X. Ding, "Acoustically excited microstructure for ondemand fouling mitigation in a microfluidic membrane filtration device," *J. Membr. Sci. Lett.*, vol. 2, no. 1, p. 100012, May 2022, doi: 10.1016/j.memlet.2021.100012.
- [31] A. Dolev, M. Kaynak, and M. S. Sakar, "Dynamics of entrapped microbubbles with multiple openings," *Phys. Fluids*, vol. 34, no. 1, p. 012012, Jan. 2022, doi: 10.1063/5.0075876.
- [32] T. A. Spelman, O. Stephan, and P. Marmottant, "Multi-directional bubble generated streaming flows," *Ultrasonics*, vol. 102, p. 106054, Mar. 2020, doi: 10.1016/j.ultras.2019.106054.
- [33] D. Gritsenko, Y. Lin, V. Hovorka, Z. Zhang, A. Ahmadianyazdi, and J. Xu, "Vibrational modes prediction for water-air bubbles trapped in circular microcavities," *Phys. Fluids*, vol. 30, no. 8, p. 082001, Aug. 2018, doi: 10.1063/1.5037328.
- [34] D. Kim, J. Hong, and S. K. Chung, "Acoustic bubble array-induced jet flow for cleaning particulate contaminants on semiconductor wafers," *Korean J. Chem. Eng.*, vol. 39, no. 12, pp. 3261–3266, Dec. 2022, doi: 10.1007/s11814-022-1214-0.
- [35] B. Behdani, S. Monjezi, J. Zhang, C. Wang, and J. Park, "Direct numerical simulation of microbubble streaming in a microfluidic device: The effect of the bubble protrusion depth on the vortex pattern," *Korean J. Chem. Eng.*, vol. 37, no. 12, pp. 2117–2123, Dec. 2020, doi: 10.1007/s11814-020-0656-5.
- [36] B. Venzac *et al.*, "PDMS Curing Inhibition on 3D-Printed Molds: Why? Also, How to Avoid It?," *Anal. Chem.*, vol. 93, no. 19, pp. 7180–7187, May 2021, doi: 10.1021/acs.analchem.0c04944.

- [37] S. D. Howkins, "Measurements of the Resonant Frequency of a Bubble near a Rigid Boundary," J. Acoust. Soc. Am., vol. 37, no. 3, pp. 504–508, Mar. 1965, doi: 10.1121/1.1909358.
- [38] A. Prosperetti, "A generalization of the Rayleigh–Plesset equation of bubble dynamics," *Phys. Fluids*, vol. 25, no. 3, pp. 409–410, Mar. 1982, doi: 10.1063/1.863775.
- [39] D. L. Miller and W. L. Nyborg, "Theoretical investigation of the response of gas-filled micropores and cavitation nuclei to ultrasound," *J. Acoust. Soc. Am.*, vol. 73, no. 5, pp. 1537–1544, May 1983, doi: 10.1121/1.389415.
- [40] D. L. Miller and E. A. Neppiras, "On the oscillation mode of gas-filled micropores," *J. Acoust. Soc. Am.*, vol. 77, no. 3, pp. 946–953, Mar. 1985, doi: 10.1121/1.392062.
- [41] T. "Leo" Liu and C.-J. "CJ" Kim, "Turning a surface superrepellent even to completely wetting liquids," *Science*, vol. 346, no. 6213, pp. 1096–1100, Nov. 2014, doi: 10.1126/science.1254787.
- [42] A. Aghakhani, A. Pena-Francesch, U. Bozuyuk, H. Cetin, P. Wrede, and M. Sitti, "High shear rate propulsion of acoustic microrobots in complex biological fluids," *Sci. Adv.*, vol. 8, no. 10, p. eabm5126, Mar. 2022, doi: 10.1126/sciadv.abm5126.
- [43] M. Wiklund, R. Green, and M. Ohlin, "Acoustofluidics 14: Applications of acoustic streaming in microfluidic devices," *Lab. Chip*, vol. 12, no. 14, p. 2438, 2012, doi: 10.1039/c2lc40203c.
- [44] A. Aghakhani, O. Yasa, P. Wrede, and M. Sitti, "Acoustically powered surface-slipping mobile microrobots." Accessed: Nov. 16, 2023. [Online]. Available: https://www.pnas.org/doi/10.1073/pnas.1920099117
- [45] P. Prentice, A. Cuschieri, K. Dholakia, M. Prausnitz, and P. Campbell, "Membrane disruption by optically controlled microbubble cavitation," *Nat. Phys.*, vol. 1, no. 2, Art. no. 2, Nov. 2005, doi: 10.1038/nphys148.
- [46] "Droplet motions fill a periodic table." Accessed: Feb. 13, 2023. [Online]. Available: https://www.pnas.org/doi/10.1073/pnas.1817065116
- [47] C. Wang, S. V. Jalikop, and S. Hilgenfeldt, "Efficient manipulation of microparticles in bubble streaming flows," *Biomicrofluidics*, vol. 6, no. 1, p. 012801, Mar. 2012, doi: 10.1063/1.3654949.
- [48] R. Bolaños-Jiménez, M. Rossi, D. F. Rivas, C. J. Kähler, and A. Marin, "Streaming flow by oscillating bubbles: quantitative diagnostics via particle tracking velocimetry," *J. Fluid Mech.*, vol. 820, pp. 529–548, Jun. 2017, doi: 10.1017/jfm.2017.229.
- [49] P. Tho, R. Manasseh, and A. Ooi, "Cavitation microstreaming patterns in single and multiple bubble systems," *J. Fluid Mech.*, vol. 576, pp. 191–233, Apr. 2007, doi: 10.1017/S0022112006004393.
- [50] H. Gelderblom, A. G. Zijlstra, L. van Wijngaarden, and A. Prosperetti, "Oscillations of a gas pocket on a liquid-covered solid surface," *Phys. Fluids*, vol. 24, no. 12, p. 122101, Dec. 2012, doi: 10.1063/1.4769179.
- [51] M. S. Plesset and A. Prosperetti, "Bubble Dynamics and Cavitation," *Annu. Rev. Fluid Mech.*, vol. 9, no. 1, pp. 145–185, 1977, doi: 10.1146/annurev.fl.09.010177.001045.
- [52] A. O. Maksimov, "Viscous streaming from surface waves on the wall of acoustically-driven gas bubbles," *Eur. J. Mech. BFluids*, vol. 26, no. 1, pp. 28–42, Jan. 2007, doi: 10.1016/j.euromechflu.2006.03.008.
- [53] M. M. Fyrillas and A. J. Szeri, "Dissolution or growth of soluble spherical oscillating bubbles," *J. Fluid Mech.*, vol. 277, pp. 381–407, Oct. 1994, doi: 10.1017/S0022112094002806.
- [54] A. Volk and C. J. Kähler, "Size Control of Sessile Microbubbles for Reproducibly Driven Acoustic Streaming," *Phys. Rev. Appl.*, vol. 9, no. 5, p. 054015, May 2018, doi: 10.1103/PhysRevApplied.9.054015.
- [55] W. L. Nyborg, "Acoustic Streaming near a Boundary," *J. Acoust. Soc. Am.*, vol. 30, no. 4, pp. 329–339, Apr. 1958, doi: 10.1121/1.1909587.
- [56] S. J. Lighthill, "Acoustic streaming," *J. Sound Vib.*, vol. 61, no. 3, pp. 391–418, Dec. 1978, doi: 10.1016/0022-460X(78)90388-7.

- [57] H.-F. Lu and W.-H. Tien, "Comparison of Acoustic Streaming Flow Patterns Induced by Solid, Liquid and Gas Obstructions," *Micromachines*, vol. 11, no. 10, p. 891, Sep. 2020, doi: 10.3390/mi11100891.
- [58] L. Ren *et al.*, "3D steerable, acoustically powered microswimmers for single-particle manipulation," *Sci. Adv.*, vol. 5, no. 10, p. eaax3084, Oct. 2019, doi: 10.1126/sciadv.aax3084.
- [59] C. Wang, B. Rallabandi, and S. Hilgenfeldt, "Frequency dependence and frequency control of microbubble streaming flows," *Phys. Fluids*, vol. 25, no. 2, p. 022002, Feb. 2013, doi: 10.1063/1.4790803.
- [60] M. R. Rasouli and M. Tabrizian, "An ultra-rapid acoustic micromixer for synthesis of organic nanoparticles," *Lab. Chip*, vol. 19, no. 19, pp. 3316–3325, 2019, doi: 10.1039/C9LC00637K.